Research Square

Preprints are preliminary reports that have not undergone peer review.
They should not be considered conclusive, used to inform clinical practice,
or referenced by the media as validated information.

# Lattice Dynamics–Driven Stability in Lead-Free Double Perovskites $Ba_2B'NbO_6$ (B' = Gd, Tb): Implications for Sustainable Photovoltaic Applications

**Neetu Malika**
KR Mangalam University
**Ruby Jindal**
ruby.jindal@krmangalam.edu.in

KR Mangalam University
**Archana Tripathi**
University of Delhi
**Rekha Rani**
Sant Longowal Institute of Engineering and Technology

**Research Article**

**Keywords:** Lead-free double perovskites, Lattice dynamics, Raman and infrared spectroscopy, Force constant model, Potential energy distribution (PED), Structural stability, Photovoltaic materials, Rare-earth substitution

**Posted Date:** November 5th, 2026

**DOI:** https://doi.org/10.21203/rs.3.rs-10613740/v1

**License:** This work is licensed under a Creative Commons Attribution 4.0 International License.
Read Full License

**Additional Declarations:** No competing interests reported.

# Abstract

Perovskite materials are at the forefront of next-generation photovoltaic technologies, yet their large-scale implementation remains limited by concerns over long-term stability and environmental impact. In this work, we present a detailed lattice dynamical study of the lead-free double perovskites $Ba_2B'NbO_6$ (B' = Gd, Tb) in the tetragonal (I4/m) structure, using normal coordinate analysis within a short-range force constant framework based on the Wilson GF matrix method. Infrared- and Raman-active phonon modes are systematically computed and assigned. Optimized stretching and bending force constants are used to quantify interatomic interactions, and potential energy distribution (PED) analysis is employed to characterize the nature of the vibrational modes. The results show that rare-earth substitution governs the lattice dynamics through a competition between mass effects and electronic contributions—particularly the higher polarizability of $Tb^{3+}$ relative to $Gd^{3+}$—leading to stronger B'–O bonding despite only weak structural distortion. High-frequency modes dominated by $NbO_6$ and $B'O_6$ octahedral stretching confirm a rigid, well-connected lattice framework. Taken together, the phonon spectra, force constants, and PED contributions point to a dynamically stable structure with strong metal–oxygen interactions and no lattice instabilities. Although the wide band gap of these oxide double perovskites limits their use as primary light absorbers, their lead-free composition, chemical stability, and tunable lattice properties make them well suited to auxiliary roles in photovoltaic architectures—such as protective layers, transport layers, and tandem device components. This study establishes a clear link between lattice dynamics, rare-earth electronic effects, and structural stability, offering design guidelines for robust, eco-friendly perovskite-based materials for real-world energy applications.


# 1. Introduction

There is a lot of interest in fundamental as well as applied research on double perovskites as they have varible optical, electrical, catalytic and thermoelectric properties [1–3]. These materials, having formula $A_2B'B''O_6$, are an ordered form of simple perovskites, with a doubled unit cell and a three-dimensional structure of corner-sharing $BO_6$ octahedra. The A-site is usually occupied by larger cations, e.g. alkaline earth metals; whereas transition metals or the rare-earth elements are located at the B' and B" locations, allowing a wide compositional range and controllability of physical properties.

The functionality of the double perovskites such as the electronic structure, optical and magnetic behavior are greatly affected by the selection and location of B-site cations [4–8]. Specifically, the f-electron interactions of rare-earth-based double perovskites produce interesting magnetic, luminescent and electronic characteristics; making them promising candidate for applications in spintronics, optoelectronics, catalysis and energy devices [9–12]. The quick evolution of photovoltaic technologies based on perovskites in recent years has increased. major doubts about the environmental effects and the sustainability of lead-containing. materials. The toxicity of lead in the traditional halide perovskites is a major problem having difficulties with large-scale deployment and secure disposal. In this respect, lead free double perovskite oxides have been found as alternatives, that are environmentally friendly and chemically stable [13, 14]. Their high ionic bonding, structural inflexibility and resistance to thermal and

chemical degradation; renders them especially attractive in terms of applications in sustainable energy. The lanthanide-based double perovskites have other benefits, such as increased stability, recyclability and alignment with the principles of green chemistry [15, 16]. Although oxide double perovskites generally have larger band gaps than the halides, restricting their use as the primary light absorbers, their good chemical stability and durability render them appropriate to auxiliary functions in photovoltaic devices including transport layers, protective layers, and units in parallel designs.

In addition to their photovoltaic applications, lanthanide double perovskites have several other applications. They possess strong magnetic ordering which enables spin-polarized transport in spintronic & magnetic storage applications, rendering them ideal for laser gain media and light-emitting diodes [17, 18]. They are capable of stabilizing due to multiple oxidation states serving as efficient catalysts in redox processes [19, 20].

Materials of this class have attracted considerable attention in the energy sector, particularly as potential cathode materials for solid oxide fuel cells (SOFCs). Their suitability arises from the combination of high ionic as well as electronic conductivity. Beyond this, they are also being explored for applications in sensing and thermoelectric devices [21–25]. Another interesting aspect is their fluorescent behaviour, which originates from f-orbital transitions, making these materials multifunctional and highly versatile [23, 24].

Among them, $Ba_2GdNbO_6$ and $Ba_2TbNbO_6$ have shown particularly promising optoelectronic and dielectric characteristics. For instance, $Ba_2GdNbO_6$ exhibits enhanced luminescence when doped with $Eu^{3+}$ ions, and further improvement has been reported with $Li^+$ co-doping [26–28]. In addition, it demonstrates significant dielectric properties [29]. Likewise, $Ba_2TbNbO_6$ is known for its tunable band gap and structural flexibility, which make it suitable for a wide range of applications, including photocatalysis, optoelectronics, and dielectric devices [30].

From a fundamental perspective, the lattice dynamics of perovskites play a crucial role in determining their stability and performance. Techniques such as Raman and infrared spectroscopy are particularly useful in probing phonon modes, which in turn provide valuable information about bonding characteristics and interatomic interactions within the crystal latticeHere, we report lattice dynamics of lead-free double perovskites $Ba_2B'NbO_6$ (B' = Gd, Tb) with a tetragonal (I4/m) crystal structure. Using normal coordinate analysis in the short-range force constant model, the Raman and infrared phonon modes are systematically calculated and assigned. The role of interatomic forces is also discussed using potential energy distribution (PED). By relating the vibrational properties to stability, this study intends to provide an insight on the suitability of the materials in safe and sustainable energy-related applications.

## 2. Material and Structural Background

The compounds $Ba_2B'NbO_6$ (B' = Gd, Tb) belong to the family of ordered double perovskite oxides and crystallize in a tetragonal structure with space group *I4/m* (No. 87) under ambient conditions. The

experimentally reported lattice parameters are *a = b = 5.9816 Å* and *c = 8.4757 Å* for $Ba_2TbNbO_6$ [31], and *a = b = 5.9985 Å* and *c = 8.5200 Å* for $Ba_2GdNbO_6$ [32].

In this structure, Ba atoms occupy the 4d Wyckoff positions (0.00, 0.50, 0.25), while oxygen atoms are distributed over two distinct sites: O1 at 8h (x, y, 0) and O2 at 4e (0, 0, z). The B-site cations, Nb and B' (Gd/Tb), are located at octahedral positions 2b (0, 0, 0.5) and 2a (0, 0, 0), respectively [31, 32]. This ordered arrangement results in alternating $NbO_6$ and $B'O_6$ octahedra, forming a three-dimensional network of corner-sharing octahedra [16, 18–20].

Each Nb and B' cation is coordinated by six oxygen atoms, forming octahedral units, while the Ba cations are surrounded by twelve oxygen atoms, leading to a distorted cuboctahedral coordination environment [34–37]. This structural arrangement plays a crucial role in determining the vibrational and bonding characteristics of the material. The crystal structure of $Ba_2B'NbO_6$ is illustrated in Fig. 1.

Group theoretical analysis for the tetragonal *I4/m* structure predicts a total of 30 zone-center phonon modes for $Ba_2B'NbO_6$ (B' = Gd, Tb). These include 3 acoustic modes and 27 optical modes. Among the optical modes, 12 are Raman-active and 15 are infrared-active. The Raman-active modes belong to the irreducible representations $A_g$, $B_g$, and $E_g$, where $A_g$ and $B_g$ are non-degenerate, while $E_g$ modes are doubly degenerate.

The detailed classification and assignment of these vibrational modes have been reported in our previous work [33]. The present study builds upon this framework to further analyze the lattice dynamics and their implications for structural stability.

# 3. Theory and Methodology

Wilson's GF matrix approach is essential for solving the Eigenvalue equation in order to determine the frequency of normal vibrations, taking into account the system's kinetic and potential energy[38]. You may find the matching Eigenvalue equation below.

$$\det | FG - E\lambda | = 0$$

Potential energies associated with vibrations are used to express the force constants matrix F, which is represented by the symbols Ki and Hi (corresponding to the stretching and bending force constants, respectively). The inverse kinetic energy matrix including masses is denoted by G. The formula $\lambda = 4\pi^2c^2v^2$, where c denotes light's velocity and v the wavenumber, yields Eigenvalues λ, which stand for frequencies. The unit matrix is indicated by E[39, 40]

Various atoms' stretching vibrational forces are governed by Hooke's law. Calculating transverse vibrations within the lattice requires consideration of both bending vibrations and stretching vibrations. A analogy between the triangle at position of equilibrium and the distorted triangle's projection onto the point of equilibrium can be used to calculate the change in a triangle's angle[41, 42].

The potential energy consists of short-range stretching vibrations (Nb-O1, Nb-O2, B’-O1, B’-O2, Ba-O1, Ba-O2) and bending vibrations (O1-Ba-O2, B’-O1-Nb). Input parameters used are Lattice constants, masses of atoms, and symmetry coordinates. In order to closely match computed and observed Raman and IR wavenumbers, the force constants for short-range bending and stretching are optimized. The Raman and infrared vibrational modes are computed using a flow chart and are given in Fig. 2:

In First step, Input Data is Prepared which Includes observed vibrational modes, internal coordinates, U matrix elements, and trial force constants to define G and F matrices.

In second step symmetry coordinate transformation is done. G and F matrices are transformed into block diagonal form to simplify calculations and correct symmetry force constants block-wise.

In step third eigenvalue equation $|FG-E\lambda|=0$ is solved to find eigenvalues and orthogonal eigenvectors. In fourth step, convergence test is done to check if calculated vibrational modes match observed values within a predefined tolerance. Stop if convergence is met.

Step five is Jacobian Matrix Formulation. If convergence is not achieved, refine force constants using the Jacobian matrix.

Step sixth is Force constant refinement. Force constants are adjusted iteratively to improve accuracy and reach convergence.

In seventh step final outcome is generated. Once refined, final vibrational modes are computed at the zone center using potential energy distribution.

Table 1 below lists the coordination and interatomic force constant values for the double perovskite oxide compound $Ba_2B'NbO_6$ (B’=Gd,Tb) in tetragonal space group[33].

Table 1
Representing position of Atoms and their Wyckoff Sites for $Ba_2B'NbO_6$ (B’=Gd,Tb) at Γ point[31, 32].

| **Atoms** | **Wyckoff sites** | **x** | | **y** | | **z** | |
|---|---|---|---|---|---|---|---|
| | | **Gd** | **Tb** | **Gd** | **Tb** | **Gd** | **Tb** |
| **Ba** | 4d | 0.0000 | 0.0000 | 0.5000 | 0.5000 | 0.2500 | 0.2500 |
| **B’** | 2a | 0.0000 | 0.0000 | 0.0000 | 0.0000 | 0.0000 | 0.0000 |
| **Nb** | 2b | 0.0000 | 0.0000 | 0.0000 | 0.0000 | 0.5000 | 0.5000 |
| **O1** | 8h | 0.2420 | 0.2441 | 0.3000 | 0.2821 | 0.0000 | 0.0000 |
| **O2** | 4e | 0.0000 | 0.0000 | 0.0000 | 0.0000 | 0.2690 | 0.2665 |

# 4. Results & Discussion

# 4.1 Vibrational Analysis

The vibrational properties of $Ba_2B'NbO_6$ (B' = Gd, Tb) were investigated using normal coordinate analysis within a short-range force constant model. A total of nine force constants, including six stretching ($K_1$–$K_6$) and three bending ($H_1$–$H_3$) interactions, were used to describe interatomic forces. The optimized force constants, bond lengths, and coordination numbers are listed in Table 2.

The study reveals that the stretching force constants of the Nb-O and B'-O bonds are much larger than Ba-O bonds, demonstrating that $NbO_6$ and $B'O_6$ octahedra constitute the rigid framework of the crystal. On the other hand, the Ba-O bonding is weaker and more ionic, resulting in the flexibility of the lattice. Such bonding is common for ordered double perovskites.

We have tabulated the Raman and infrared-active phonon modes in Table 3. The modes are grouped into Ag, Bg, and Eg (Raman) and Au and Eu (infrared) as expected from group theoretical analysis of the tetragonal I4/m space group. The calculated frequencies agree well with the experimental data of compounds of similar structure (e.g., $Sr_2CoWO_6$), justifying the model. The vibration spectrum can be classified into three regions- High-frequency modes (> 500 $cm^{-1}$), which originates from stretching vibrations of metal-oxygen bonds of the $NbO_6$ and $B'O_6$ octahedra, corresponding to the bond strength, shows strong bonding and rigid lattice. Medium-frequency modes are associated with bending vibrational modes of the octahedral clusters and low-frequency modes (< 200 $cm^{-1}$) are dominated with lattice vibrations involving large ions such as Ba and rare-earth elements. Potential energy distribution (PED) calculations (Table 4) help detemine the nature of these modes. Very-high-frequency modes, such as $Ag_1$ at 870 $cm^{-1}$, are mainly dominated by metal-oxygen interactions, which help in maintaining the stiffness of the octahedra. Medium-frequency modes, such as $Ag_5$ (500 $cm^{-1}$) display the mixed stretching and bending interactions, and low-frequency modes (e.g. $Ag_4$ 200 $cm^{-1}$) are dominated by lattice vibrations. Overall, the vibrational modes depend on the bonding and connectivity of the $NbO_6$ and $B'O_6$ octahedra, giving rise to the stability of the lattice.

# 4.2 Effect of Rare-Earth Substitution

Replacing rare-earth ions, $Gd^{3+}$ by $Tb^{3+}$ has a subtle impact on lattice dynamics. The compounds are isostructural but there are differences due to atomic mass and electronic structure. For simple ionic solids, a smaller ionic radius means shorter and stronger bonds. According to Table 2, Tb-O bond (1.9790 Å) is a little bit longer than the Gd-O (1.9681 Å) but with larger force constant. This suggests that bonding is not only dependent on ionic size but also on electronic factors.

This is due to the electronic structures of the ions. $Gd^{3+}$ has a stable half-filled $4f^7$ configuration, which is not very polarizable. In contrast, $Tb^{3+}$ having $4f^8$ is more polarizable, leading to stronger bonding with the oxygen atoms. This greater polarizability leads to a stronger effective bond with oxygen than in the Tb-O case, although the bond length is slightly longer.

The GF matrix model can be used to explain this as a result of both mass and bond strength effects. The G matrix accounts for mass, with Tb having a higher mass than La; this would lead to vibrational frequencies ($\nu \propto 1/\sqrt{\mu}$). The F matrix represents the force constants, and with stronger Tb O interactions tend to increase frequencies. The balance between the two effects results in nearly unchanged or even increased frequencies for some modes.

Using the GF matrix model, this can be explained as a combination of mass and bond strength effects. The G matrix represents mass, with the larger mass of Tb expected to result in vibrational frequencies ($\nu \propto 1/\sqrt{\mu}$). But the F matrix accounts for the stiffness of bonds, and the stronger Tb–O interactions tend to increase frequencies. The competition between these effects leads to almost unchanged or even higher frequencies for certain modes. For instance, the $Bg_1$ from 669.7 $cm^{-1}$ to 672.4 $cm^{-1}$, and the $Eu_3$ mode shifts from 193.3 $cm^{-1}$ to 197.8 $cm^{-1}$. Finally, stiffening of lattice is also observed. B' - O force constants stiffen, force constants of Nb-O bonds decrease slightly, suggesting cooperative response of the octahedra. Ba-O forces remain unchanged, implying the A-site environment is not affected by substitution.

Crucially, the fundamental mode of vibration of the $NbO_6$ octahedra is preserved. The highest frequency $Ag_1$ mode (870 $cm^{-1}$) associated with the symmetric stretching of octahedra mode stays the same, which means that the structure is stable. This suggests that rare-earth doping leads to local effects without affecting the stability of the lattice. These findings are consistent with the behavior of rare-earth substituted perovskites, in which electronic structure, polarizability and crystal field effects significantly affect lattice and phonon behavior.

# 4.3 Implications for Stability and Photovoltaics

The lattice dynamics of $Ba_2B'NbO_6$ plays an important role when considering their structural photovoltaic applications. The constraints of the rigid $NbO_6$ and $B'O_6$ octahedra structure is stability, and is needed to avoid thermal and environmental instability. This is critical for photovoltaic devices. At the same time, weaker Ba-O bonds provide some structural flexibility to tolerate some distortion to the structure to allow strain and defects to be accommodated within the structure. The rigid $NbO_6$ and $B'O_6$ octahedral structure provides a high lattice stability, and is required for thermal and environmental degradation. This is a essential for practical photovoltaic devices.

At the same time, weaker Ba-O bonds provide some structural flexibility to tolerate some distortion to the structure to allow strain and defects to be accommodated within the structure and flexibility increases defect tolerance, a key factor in minimizing and flexibility increases defect tolerance, a key factor in minimizing recombination losses in photovoltaic materials. Function is also optimized by doping with rare-earth ions. The increased polarizability of $Tb^{3+}$ can increase the dielectric screening and so help to stabilize charge carriers and decrease recombination.

At the same time, the absence of soft phonon modes can be expected to lead to a lattice ensures that the material will not undergo a phase transition during operation. Although oxide double perovskites are

likely to have a higher band gap and not absorb light absorbers, their stability provides the possibility for other materials in photovoltaics. These include transport layers, protective coatings, and components in tandem architectures.

Furthermore, the ability to tune vibrational properties through rare-earth substitution provides a pathway for engineering thermal and electronic behaviour. Phonon tuning can assist with thermal conduction, and improve the device stability and reliability in operation.

In conclusion, the balance among octahedral rigidity, lattice flexibility and rare-earth electronic states determines the stability and functionality of $Ba_2B'NbO_6$ compounds. These characteristics render them as potential eco-friendly, lead-free materials for future energy and photovoltaic devices.

# 5. Real-World Relevance and Sustainability

Perovskite materials for energy applications must compromise among performance, stability, environmental compatibility and manufacturability. In this regard, lead-free double perovskites $Ba_2B'NbO_6$ (B' = Gd, Tb) that can replace the conventional lead-based materials is promising. Removing lead reduces the risk and allows its safe use in large quantities and recycling after use. The findings of the lattice-dynamical analysis carried out in this study indicate the materials' structural stability. The strong Nb-O and B'-O interactions, observed in high-frequency vibrational modes and high force constants, are in agreement with the stiff octahedral rigid network. However, the flexible Ba-O interactions allow the lattice to be pliable. This combination of stiffness and flexibility is desirable from the practical point of view in the sense that the material is exposed to thermal vibrations, mechanical strain and other environmental conditions. The absence of soft modes also implies dynamic stability, with little chance of structural instabilities or phase transformations.

An important finding of this study is how lattice doping affects its structure. The increase in polarizability (from $Gd^{3+}$ to $Tb^{3}$) increases the B' -O interconnectivities and slightly alters the phonon behavior, without affecting the structure. This demonstrates the ability to modulate the phonons and structure on the atomic scale through doping, and thus to enable control over thermal, dielectric and defect tolerance. Oxide double perovskites, although having larger band gaps, are not the most desirable primary photo absorbers, their stability makes them ideal materials in substitute roles in solar cells. For example, charge transport, buffer, protective and tandem solar cell layers, in which stability is essential. From an environmental viewpoint, these materials are useful in utilizing a reasonably cheap and recyclable elements, and the conventional oxide fabrication techniques. Their stability reduces degradation and replacement requirements, and therefore lifecycle cost and environmental footprint. To conclude, this study shows that $Ba_2B'NbO_6$ double perovskites have a high degree of structural stability, can be tuned in terms of phonon dynamics, and are environmentally sustainable, and are therefore promising materials for sustainable energy technologies under harsh environmental conditions.

# 6. Conclusion

In the present study, a comprehensive lattice dynamical study of lead-free double perovskites $Ba_2B'NbO_6$ (B' = Gd, Tb) has been carried out using normal coordinate analysis within a short-range force constant framework. The Raman- and infrared-active phonons have been been calculated and assigned, with the results in good agreement with the experimental structurally similar species, thus confirming the accuracy of the chosen approach.

The interatomic force constants and potential energy distribution analyses show that the vibrations are mainly dominated by the metal-oxygen interactions in $NbO_6$ and $B'O_6$ octahedra.

The occurrence of high-frequency stretching modes and distinct bonding vibrations, reveals the presence of a stiff and dynamically robust lattice. At the same time, weaker Ba–O interactions provide necessary structural flexibility, ensuring a balanced lattice response.

Another aspect of lattice dynamics highlighted in this work is rare-earth substitution. The studies comparing $Gd^{3+}$ and $Tb^{3+}$ show that the vibrational characteristics depend not only on mass, electronic structure and polarizability. The increased bonding between Tb–O ions tend to compensate for dynamical mass effects, leading to dynamic changes but not affecting stability. For real application, the strong bonding, absence of "soft" phonons and stability suggests the materials will be stable under normal thermal and environmental conditions.

Although $Ba_2B'NbO_6$ compounds may not be able to absorb light directly because of the large free, stable and high lattice tunability make them exciting materials that can play supporting roles in PV devices, such as transport layers, buffer or coating layers and tandem devices. In conclusion, this work establishes a connection between the lattice dynamics, electronic structure and the stability in double perovskites. The results will be used to create new non-toxic and stable and multifunctional materials, which will allow design of new generation sustainable photovoltaic and energy devices.

Table 2

Interatomic Force Constant (FC) Values (in $10^2$ N/m) with Coordination Number (CN) for Ba2B'NbO6 (B'=Gd,Tb) compounds in I4/m structure

| **$Ba_2GdNbO_6$** | | | | | **$Ba_2TbNbO_6$** | | | | |
|---|---|---|---|---|---|---|---|---|---|
| FC | Between atoms | CN | Distance (**Å**) /angles (°) | FC value (N/cm) | FC | Between atoms | CN | Distance (**Å**) /angles (°) | FC value (N/cm) |
| $K_1$ | Nb-O1 | 4 | 1.9582 | 1.650 | $K_1$ | Tb-O2 | 2 | 1.9790 | 1.960 |
| $K_2$ | Gd-O2 | 2 | 1.9681 | 1.470 | $K_2$ | Nb-O1 | 4 | 2.0104 | 1.420 |
| $K_3$ | Nb-O2 | 2 | 2.2919 | 1.420 | $K_3$ | Tb-O1 | 4 | 2.2314 | 0.980 |
| $K_4$ | Gd-O1 | 4 | 2.3121 | 0.690 | $K_4$ | Nb-O2 | 2 | 2.2586 | 0.960 |
| $K_5$ | Ba-O2 | 8 | 3.0036 | 0.140 | $K_5$ | Ba-O2 | 8 | 2.9941 | 0.140 |
| $K_6$ | Ba-O1 | 8 | 3.1891 | 0.070 | $K_6$ | Ba-O1 | 8 | 3.1112 | 0.060 |
| $H_1$ | O1-Ba-O2 | 8 | 117.999 | 0.050 | $H_1$ | O1-Ba-O2 | 8 | 118.121 | 0.963 |
| $H_2$ | O1-Ba-O2 | 8 | 117.499 | 1.010 | $H_2$ | O1-Ba-O2 | 8 | 119.057 | 0.990 |
| $H_3$ | O1-Gd-Nb | 4 | 166.675 | 0.042 | $H_3$ | O1-Tb-Nb | 4 | 171.284 | 0.050 |

Table 3

Presently computed Raman and IR zone-center vibrational modes for $Ba_2B'NbO_6$ (B'=Gd,Tb), along with experimentally determined modes (in $cm^{-1}$) of similar compounds and $Sr_2CoWO_6$ [43]

| **Species** | **Wave numbers as Observed by Manoun et al for $Sr_2CoWO_6$ (in $cm^{-1}$) [46]** | **Presently calculated wave numbers for $Ba_2GdNbO_6$ (in $cm^{-1}$)** | **Presently calculated wave numbers for $Ba_2TbNbO_6$ (in $cm^{-1}$)** |
|---|---|---|---|
| $A_{g1}$ | 864.0 | 870.3 | 869.9 |
| $A_{g2}$ | 572.0 | 515.1 | 521.4 |
| $A_{g3}$ | 225.0 | 234.0 | 227.1 |
| $B_{g1}$ | 716.0 | 669.7 | 672.4 |
| $B_{g2}$ | | 297.5 | 291.3 |
| $B_{g3}$ | 134.0 | 133.7 | 138.4 |
| $E_{g1}$ | 312.0 | 385.6 | 388.8 |
| $E_{g2}$ | | 149.5 | 150.5 |
| $E_{g3}$ | | 94.30 | 95.1 |
| $A_{u1}$ | | 813.6 | 817.0 |
| $A_{u2}$ | | 271.8 | 271.7 |
| $A_{u3}$ | | 201.0 | 192.8 |
| $A_{u4}$ | | 60.4 | 55.8 |
| $B_u$ | | 183.1 | 189.6 |
| $E_{u1}$ | | 707.6 | 707.0 |
| $E_{u2}$ | | 374.2 | 360.0 |
| $E_{u3}$ | | 193.3 | 197.8 |
| $E_{u4}$ | | 149.7 | 168.5 |
| $E_{u5}$ | | 92.8 | 97.7 |

Table 4
Represents major Contributions of Force Constants according to Potential Energy Distribution (PED) for the $Ba_2B'NbO_6$ (B'=Gd,Tb) compounds

| Species | Calculated wavenumbers for $Ba_2GdNbO_6$ | Major contributions of two dominant Force constants as per PED | | | |
|---|---|---|---|---|---|
| | | $Ba_2GdNbO_6$ | | $Ba_2TbNbO_6$ | |
| $A_{g1}$ | 870.3 | H2 = 61% | K2 = 14% | H2 = 59% | K1 = 19% |
| $A_{g2}$ | 515.1 | K1 = 45% | K4 = 19% | K2 = 38% | K1 = 23% |
| $A_{g3}$ | 234.0 | H3 = 31% | H2 = 16% | H3 = 40% | H2 = 14% |
| $B_{g1}$ | 669.7 | H2 = 52% | K1 = 32% | H2 = 50% | K2 = 28% |
| $B_{g2}$ | 297.5 | K1 = 35% | H2 = 35% | H2 = 36% | K2 = 26% |
| $B_{g3}$ | 133.7 | K6 = 42% | H3 = 37% | H3 = 47% | K3 = 35% |
| $E_{g1}$ | 385.6 | H2 = 88% | K5 = 10% | H2 = 88% | K5 = 10% |
| $E_{g2}$ | 149.5 | K5 = 80% | K6 = 11% | K5 = 80% | H2 = 8% |
| $E_{g3}$ | 94.30 | H1 = 51% | K6 = 46% | H1 = 57% | K6 = 41% |
| $A_{u1}$ | 813.6 | H2 = 50% | K3 = 24% | H2 = 50% | K1 = 32% |
| $A_{u2}$ | 271.8 | K3 = 41% | H2 = 39% | H2 = 40% | K1 = 38% |
| $A_{u3}$ | 201.0 | K2 = 63% | K3 = 34% | K4 = 71% | K1 = 29% |
| $A_{u4}$ | 60.4 | K6 = 92% | H2 = 5% | K6 = 93% | H2 = 4% |
| $B_u$ | 183.1 | H2 = 73% | K6 = 20% | H2 = 76% | K6 = 16% |
| $E_{u1}$ | 707.6 | H2 = 52% | K1 = 33% | H2 = 50% | K2 = 29% |
| $E_{u2}$ | 374.2 | K1 = 46% | H2 = 35.;% | K2 = 38% | H2 = 35% |
| $E_{u3}$ | 193.3 | K5 = 38% | K4 = 23% | K3 = 28% | K5 = 27% |
| $E_{u4}$ | 149.7 | K4 = 47% | H3 = 19% | K3 = 35% | H3 = 23% |
| $E_{u5}$ | 92.8 | K5 = 30% | H3 = 24% | K5 = 32% | K7 = 25% |

# Declarations

# Author Contribution

All author has equal contribution

# References


1. Kobayashi KI, Kimura T, Sawada H, Terakura K, Tokura Y (1998) Room-temperature magnetoresistance in an oxide material with an ordered double-perovskite structure. Nature 395:677–680
2. Mahato R, Sethupathi K, Venkataraman S (2010) Colossal magnetoresistance in the double perovskite oxide $La_2CoMnO_6$. J Appl Phys. ;107
3. Sarma DD, Mahadevan P, Saha-Dasgupta T, Ray S, Kumar A (2000) Electronic structure of $Sr_2FeMoO_6$. Phys Rev Lett 85:2549–2552
4. Arumugam GM, Karunakaran SK, Galian RE, Pérez-Prieto J (2022) Recent progress in lanthanide-doped inorganic perovskite nanocrystals and nanoheterostructures: A future vision of bioimaging. Nanomaterials 12:2130
5. Smerechuk A, Morrow R, Wurmehl S, Sidletskiy O (2021) Synthesis of magnetically frustrated oxides with double perovskite structure. Acta Crystallogr A 77:C428
6. Saha-Dasgupta T (2020) Double perovskites with 3d and 4d/5d transition metals: Compounds with promise. Mater Res Express 7:014003
7. Vasala S, Karppinen M (2015) $A_2B'B''O_6$ perovskites: A review. Prog Solid State Chem 43:1–36
8. Sarma DD, Sampathkumaran EV, Ray S, Nagarajan R, Majumdar S, Kumar A et al (2000) Magnetoresistance in ordered and disordered double perovskite oxide $Sr_2FeMoO_6$. Solid State Commun 114:465–468
9. McClure ET, Ball MR, Windl W, Woodward PM (2016) $Cs_2AgBiX_6$ (X = Br, Cl): New visible light absorbing lead-free halide perovskites. Chem Mater 28:1348–1354
10. Mahmoud N, Khalifeh J, Mousa A (2019) Effects of rare earth Eu on structural and optical properties of $SrLiF_3$. Phys B
11. Mubarak AA (2014) Ab initio study of structural and optical properties of $SrXF_3$ compounds. Comput Mater Sci 81:478–482
12. Mousa A, Jaradat R, Abu-Jafar M, Mahmoud N, Al-Qaisi S, Khalifeh J et al (2020) Structural and elastic properties of $TM_3In$ compounds. AIP Adv. ;10
13. Wang M, Wang W, Ma B, Shen W, Liu L, Cao K et al (2021) Lead-free perovskite materials for solar cells. Nano-Micro Lett. ;13
14. Jindal R, Tripathi A, Mohan C, Garg A, Varma RS (2024) Lead-free halide double perovskites for sustainable applications. Chem Phys Impact 9:100770
15. Schileo G, Grancini G (2021) Lead or no lead? Sustainability of perovskite solar cells. J Mater Chem C 9:67–76

16. Wei H, Huang J (2019) Halide perovskites for radiation detection. Nat Commun 10:1066
17. Zhao S, Yamamoto K, Iikubo S, Hayase S, Ma T (2018) Electronic and optical properties of $Cs_2NaBX_6$. J Phys Chem Solids 117:117–121
18. Zhou J, Rong X, Molokeev MS, Zhang X, Xia Z (2018) Optical properties of $Cs_2AgSbCl_6$. J Mater Chem A 6:2346–2352
19. Kumar S, Singh M, Pal R, Azad UP, Singh AK, Singh DP et al (2021) Lanthanide-based double perovskites as catalysts. Int J Hydrog Energy 46:17163–17172
20. Singh DP, Mukherjee S, Bhagat S, Singh N, Singh M, Singh AK et al (2024) Lanthanum-based perovskites for oxygen reactions. Int J Hydrog Energy 51:587–600
21. Wu C, Zhang Q, Liu Y, Luo W, Guo X, Huang Z et al (2018) Lead-free double perovskite $Cs_2AgBiBr_6$ film. Adv Sci 5:1700759
22. Wu H (2001) Electronic structure of double perovskites. Phys Rev B. ;64
23. Li J, Xiao J, Lin T, Yan Z, Han X (2022) Luminescence in layered double perovskites. J Mater Chem C 10:7626–7632
24. Xu H, Yu J, Hu Q, Han Q, Wu W (2023) Photoluminescence in doped double perovskites. Mater Today Chem 30:101580
25. Mahmoud N, Mousa A, Shaheen A (2022) Thermoelectric perovskite oxides study. Int J Energy Res. ;46
26. Zhang X, Cui R, Zhang J, Yuan G, Qi X, Deng C (2021) Photoluminescence of $Ba_2GdNbO_6$:$Sm^{3+}$. Optik 245:167646
27. Khouidmi A, Dahou FZ, Baltach H, Laref A, Monir M (2022) Properties of $Ba_2GdNbO_6$. Philos Mag 103:1–20
28. Rezende MVS, Valério MEG, Mouta R, Diniz EM, Paschoal CW (2014) Luminescent enhancement in $Ba_2GdNbO_6$:$Eu^{3+}$. arXiv
29. Structural and dielectric properties of doped $CoNb_2O_6$. ResearchGate
30. Roy DC, Matsukawa M, Yonai T, Arakida M, Taniguchi H, Nishidate K et al (2023) Photocatalytic $Ba_2Tb(Bi,Sb)O_6$. J Mater Sci Mater Electron 34:281
31. Saines PJ, Kennedy BJ, Elcombe MM (2007) Structure of $Ba_2LnB'O_6$. J Solid State Chem 180:401–409
32. Fu WT, IJdo DJW (2006) Structure of $Ba_2LnNbO_6$. J Solid State Chem 179:1022–1028
33. Malik N, Jindal R, Tripathi A, Kumari N (2024) Lattice dynamics of $Sr_2B'WO_6$. Chem Phys Impact 9:100776
34. Dhilip M, Marimuthu M, Sundaramurthy R, Jayalakshmi V, Venugopalan A, Krishnaswamy S (2019) $SrCoO_3$ perovskite synthesis. J Mater Sci Mater Electron. ;30
35. Ayala AP (2007) Raman study of $A_2CoBO_6$. J Appl Phys 101:123511
36. Viola M, Martínez-Lope MJ, Alonso JA, Martínez JL, De Paoli JM, Pagola S et al (2003) $Sr_2CoWO_6$ Struct ChemInform. ;34

37. Saadon NAFM, Ali NM, Ibrahim N, Mohamed Z (2021) $Sr_2NiWO_6$ properties. AIP Conf Proc. ;2368:030006
38. Shimanouchi T, Tsuboi M, Miyazawa T (1961) GF-matrix method. J Chem Phys 35:1597–1613
39. Saini N, Jindal R, Tripathi A (2023) Influence of B-site cation in lattice dynamics of bilayered Ruddlesden–Popper Sr3B2O7 (B = Zr, Mo, Sn, Hf) compounds. J Raman Spectrosc 54:847–856
40. Jindal R, Sinha MM, Gupta HC (2013) Study of zone center phonons in wolframite $ZnWO_4$. Turk J Phys 37:107–112
41. Jindal R, Sinha MM, Gupta HC (2013) Lattice vibrations of $AVO_4$ crystals. Spectrochim Acta A 113:286–290
42. Gupta HC, Ruby, Sinha MM (2012) A Lattice Dynamical Investigation of the Raman and the Infrared Wave Numbers of $MnWO_4$. Acta Phys Pol A 122:142–145
43. Siqueira JM, Martinez LG, Freire PTC, Souza Filho AG, Alves JPS, Ayala AP et al (2023) Raman study of orthoferrites. Sci Rep 13:22563
44. Argyriou DN, Radaelli PG, Bordallo HN, Blake GR, Palstra TTM (2000) Rare-earth substitution in $REMnO_3$. Phys Rev B 61:15269–15275
45. Iliev MN, Lee HG, Popov VN, Litvinchuk AP, Sun Y, Thomsen C et al (2006) Spin–phonon coupling in $RMnO_3$. Phys Rev B 73:064302
46. Manoun B, Igartua JM, Gateshki M, Saxena SK (2008) High-pressure study of $Sr_2CoWO_6$. J Mol Struct 888:244–252

# Figures

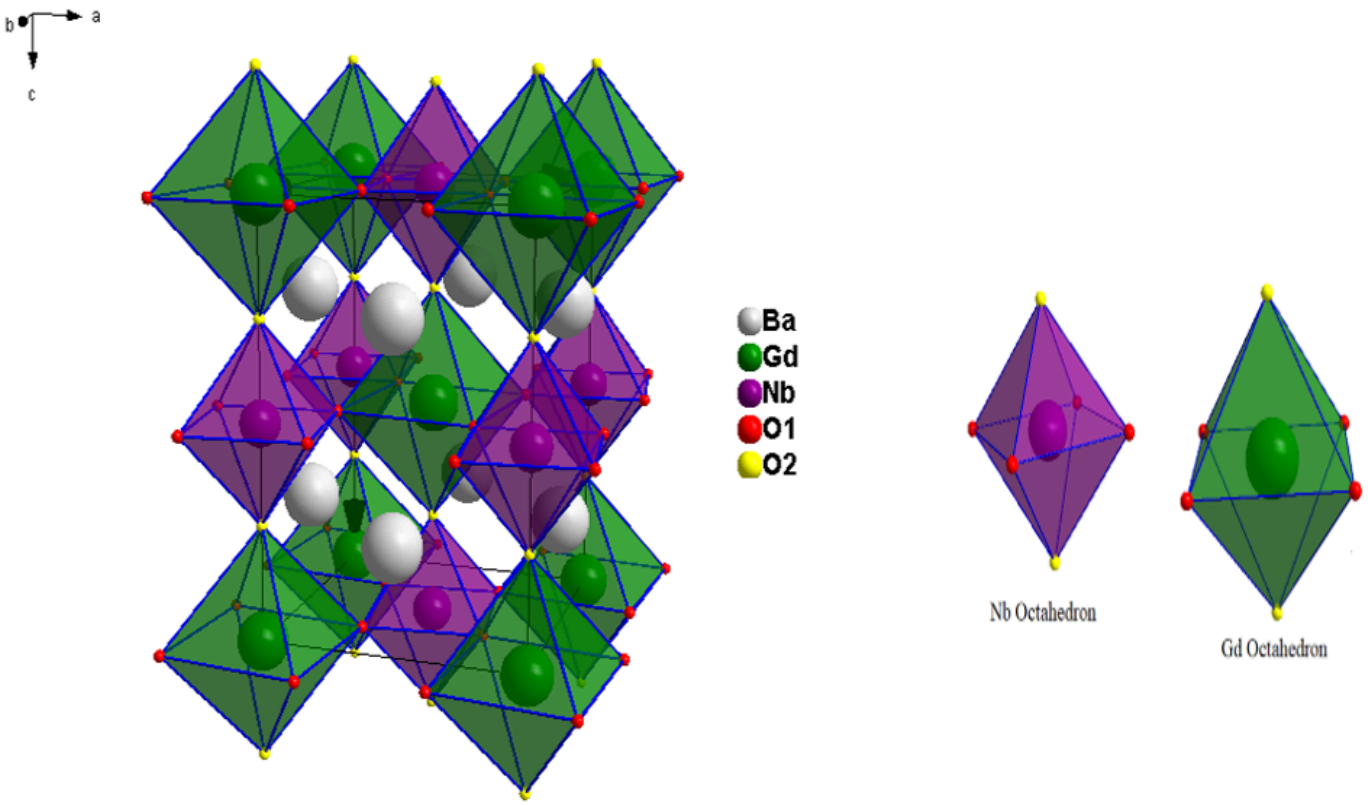
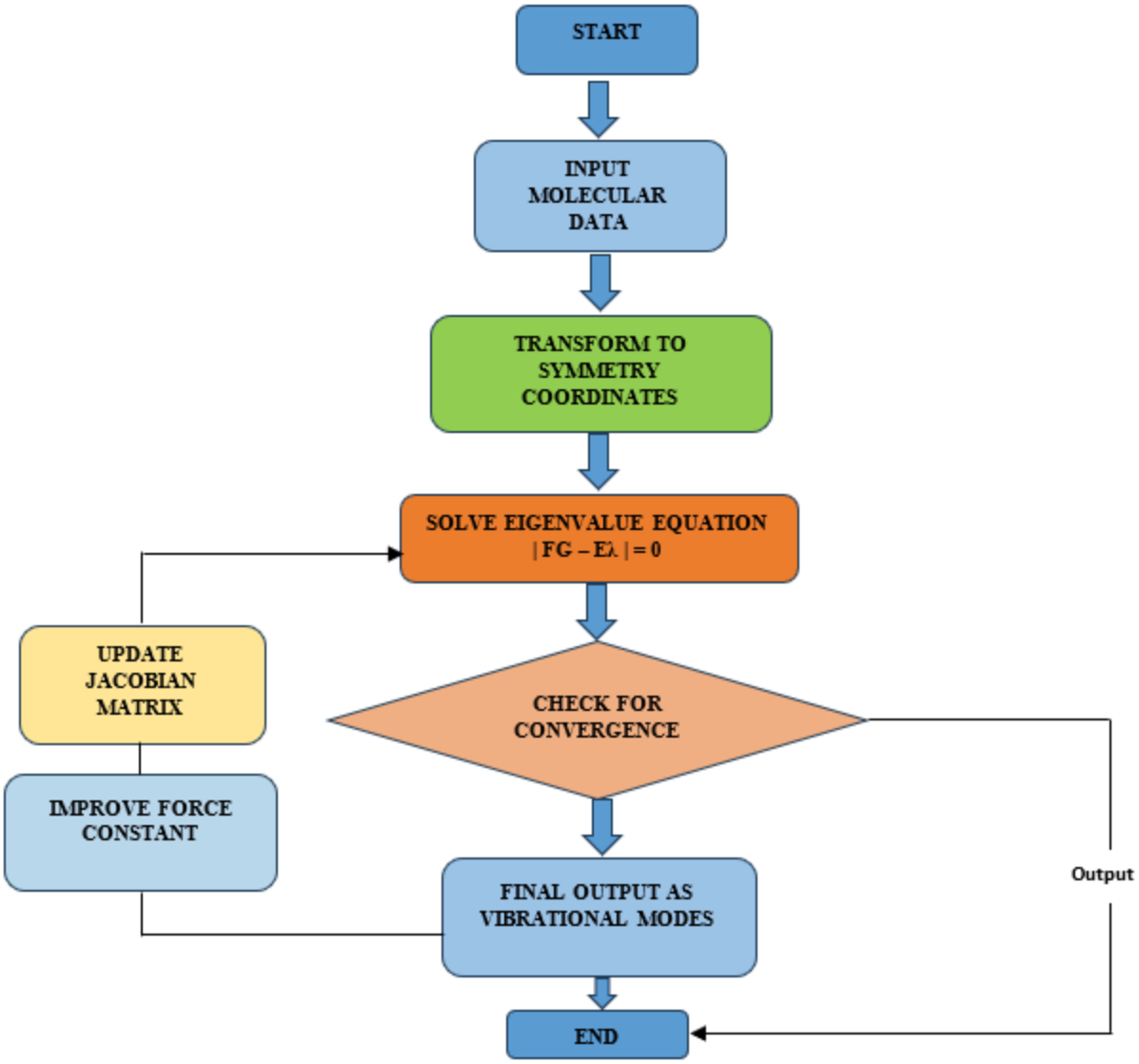



**Figure 1**

Crystal structure of $Ba_2GdNbO_6$ (Made using Diamond software)




## Figure 2

Flow chart for the calculation of Raman and infrared vibrational modes